The following publication Ren, Y., Zhou, X., Tang, J., Ding, J., Chen, S., Zhang, J., Hu, T., Yang, X.-S., Wang, X., & Yang, J. (2019). Boron-Doped Spherical Hollow-Porous Silicon Local Lattice Expansion toward a High-Performance Lithium-Ion-Battery Anode. Inorganic Chemistry, 58(7), 4592-4599 is available at https://doi.org/10.1021/acs.inorgchem.9b00158.

Boron Doped Spherical Hollow Porous Si Local Lattice Expansion towards High Performance Li-ion Batteries Anode

Yongpeng Ren [a], *Xiangyang Zhou* [a], *Jingjing Tang* [a], *Jing Ding* [a], *Song Chen* [a], *Jiaming Zhang* [a], *Tingjie Hu* [a], *Xu-Sheng Yang* [b]*, *Xinming Wang* [c] *and Juan Yang* [a]*

[a] School of Metallurgy and Environment, Central South University, Changsha 410083, China.
[b] Advanced Manufacturing Technology Research Centre, Department of Industrial and Systems Engineering, The Hong Kong Polytechnic University, Hung Hom, Kowloon, Hong Kong, China
[c] School of Materials Science and Engineering, Xiangtan University, Xiangtan, China

*Corresponding author.
[a*] E-mail: j-yang@csu.edu.cn, (J. Yang)
[b*] E-mail: xsyang@polyu.edu.hk, (X. Yang)

KEYWORDS: Si anode, Li-ion batteries, lattice expansion, boron doping

ABSTRACT: Silicon (Si) attracts extensive attention as the advanced anode material for the Lithium (Li)-ion batteries (LIBs), due to the ultra-high Li storage capacity and suitable voltage plateau. Hollow porous structure and dopant-induced lattice expansion can enhance the cyclic stability and the transporting kinetics of Li-ions. However, it is still difficult to synthesize the Si anode possessing these structures simultaneously by a facile method. Herein, lightly boron doped spherical hollow porous Si (B-HPSi) anode material for LIBs is synthesized by a facile magnesiothermic reduction from boron doped silica. The B-HPSi exhibits local lattice expansion located on boundaries of refined subgrains. Boron atoms in silicon

contribute to the increase of the conductivity and the expansion of lattices. Based on the first principles calculations, the B dopants induce the conductivity increasing and the local lattice expanding. As a result, B-HPSi electrodes exhibit high specific capacity of ~1500 mAh g^{-1} at 0.84 A g^{-1} and maintains 93% after 150 cycles. The reversible capacities of ~1250 mAh g^{-1}, ~1000 mAh g^{-1} and ~800 mAh g^{-1} can be delivered at 2.1 A g^{-1}, 4.2 A g^{-1} and 8.4 A g^{-1}, respectively.

INTRODUCTION

Advanced anode materials of Lithium (Li)-ion batteries (LIBs) require high specific capacity and cyclic stability.[1, 2] Owing to the ultra-high Li storage capacity (3579 mAh g^{-1} for $Li_{3.75}Si$) and suitable voltage plateau, silicon (Si) has attracted extensive attention as the advanced anode material among numerous candidates Moreover, a plenty of works have been devoting to fabricate the elaborate and effective structures to improve the performance of ionic transfer of Si anode.[3-12] It is believed that the existence of hierarchical pores and gaps in Si can provide the interconnected paths for Li ion transporting.[4, 13, 14] Besides, it has also been found that the hollow porous structured Si can partially reduce violent capacity degradation, prevent pulverization and stabilize the solid electrolyte interface (SEI) films, which is attributed to the alleviation of the drastic volume change of Si during cycling.[4, 15]

However, the improvement of intrinsic capability of transmission dynamics for Li-ions of Si anodes is rarely reported. Previous studies indicated that the dopant in Si could also induce some specific lattice deformations, including intra-crystalline deformation and surface deformation. These dopant induced deformation could lead to the fluctuation of energy barriers, thereby potentially providing the lower energy barriers for the faster Li diffusion pathways.[16-18] Based on the classical research, dopant can also increase the carrier concentration and correspondingly, the electronic conductivity of Si.[19, 20] For example, some works found that Boron (B) doped Si anodes possess the better transferring performance than the un-doped ones, partially because of the improved electronic and ionic conductivity.[21-23] In addition, the locally elongated bond could expand the framework of Si, which can further improve the transporting kinetics of Li-ions.[16] Recently, it has also been found that the disordered amorphous Si can contribute to the improvement of the rate performance and cycling stability.[24, 25] Therefore, synthesizing porous Si materials with lattice deformations (expansion) should be of significance for enhancing the Li-ions transferring rate and cycling stability. To simultaneously obtaining hollow, porous and doped features, magnesiothermic reduction is used for fabricating Si materials.[26, 27] By using this methodology, for example, Favors et al and Zuo et al successfully obtained the hollow porous Si products based on the conformal Mg reductions from various SiO_2.[26, 27] However, magnesiothermic reductions are still suffering the disintegration of designed morphology, even though they are elaborate.[28, 29] On the other hand, the traditional doping methods which highly rely on the top-down bulk diffusion or expensive vapor deposition methods, have never been integrated into the magnesiothermic reductions.

Herein, we develop a facile strategy in the present work for the fabrication of the boron doped hollow porous nanostructured Si (B-HPSi) anode with lattice expansion areas between sub-grains via the co-condensation and Mg reduction. In the co-condensation stage, B doped hollow SiO_2 spheres (B-HSiO_2) are obtained through a modified Stöber method combined with water etching process. Then, B-HSiO_2 spheres are converted to B-HPSi spheres. Besides, B dopant induces local lattice expansion and sub-grains refining, contributing to the improvement of rate performance and cyclic stability. More specifically: firstly, the hollow porous nano-structures and the local lattice expansion provide the hierarchical ion transportation paths, which not only shorten the ion transmission distance, but also improve the intrinsic capability of ion conductivity in solid phase;[30] secondly, this structure provides a remarkable accommodation of the volume change, improving the structural and interfacial stabilities against cycling; thirdly, Si sub-grains are refined due to the stress and strain fields induced by B atoms, which may further reduce the volume change during cycling. B-HPSi materials deliver high specific capacity of ~1500 mAh g^{-1} and retention capacity of 93% at 0.84 A g^{-1} over 150 cycles, and excellent cycling stability of 850 mAh g^{-1} at 4.2 A g^{-1} after 400 cycles. In addition, the new associated synthesizing method for the B doped hollow SiO_2 through a boric acid involved Stöber method will provide new insight into fabricating stable high-capacity energy storage materials toward practical application.

EXPERIMENTAL SECTION

Synthesis of materials: First, 9 mL tetraethyl orthosilicate (TEOS) and 0.32 g boric acid were dissolved in 91 mL absolute methanol under vigorously stirring for 10 min. Then, 0.1 mL diluted HCl (0.012 mol L^{-1}) was injected to this solution, which was heated to 60 °C under stirring for another 3 h. After being cooled to room temperature, the mixture was injected to another solution of ammonia solution (18 mL, 25wt%), deionized water (49.5 mL) and methanol (32.5 mL). The hydrolysis reaction proceeded at room temperature for 3 h under vigorous stirring and then aged overnight. The resultant white emulsion was alternately centrifuged and washed with ethanol and water. The precipitate was dispersed into water and aged at 70 °C for 30 min. After drying, the white powder was calcined at 550 °C for 2 h in air to obtain B-HSiO$_2$. To prepare B-HPSi, 1 g as-prepared B-HSiO$_2$ nanoparticles were mixed with 10 g NaCl and 0.9 g Mg powder, then sealed in a brass reactor, placed in a horizontal tube furnace, heated to 700 °C and finally kept for 6 h under Ar atmosphere. The B-HPSi nanoparticles were obtained after being washed with HCl (1mol L^{-1}) and 5% HF solution, and dried at 60 °C. The reference samples were synthesized via the same method by altering the amount of boric acid during the fabrication of SiO$_2$. The obtained SiO$_2$ nanoparticles without boric acid, with 0.08 g and 0.16 g boric acid were marked as B0-SiO$_2$, B1-SiO$_2$ and B2-SiO$_2$. Correspondingly, the obtained Si products were denoted as B0-Si, B1-Si and B2-Si.

Characterization: Morphologies and microstructures of samples were characterized with field emission scanning electron microscopy (SEM, Nova NanoSEM230) operated at acceleration voltage of 15 kV, and field emission transmission electron microscopy (TEM, JEM-2100F) operated at acceleration voltage of 200 kV. Phase structures were characterized by X-ray diffraction (XRD, Rigaku-TTRIII) with Cu Ka radiation at a scanning rate of 10 °/min. X-ray photoelectron spectroscopy (XPS) was performed on ESCALAB 250Xi (Thermo Fisher-VG Scientific). Element content was detected by inductively coupled plasma atomic emission spectroscopy (ICP-AES Baird PS-6). Nitrogen adsorption and desorption isotherms were collected at -196 °C under the pressures of 0.05-0.99 P/P_0 using ASAP 2020. Specific surface areas and pore size distributions of B-HPSi were calculated by Brunauer–Emmett–Teller (BET) method and Barrett–Joyner–Halenda (BJH) method, respectively.

Cell Assembly and Electrochemical Testing: Working electrodes were prepared by casting the slurry with a weight ratio of Si: acetylene black: sodium alginate = 6:2:2 in deionized water on a copper foil. The mass loading of the electrode ranges from 0.5 to 1mg/cm^2. The electrode was thoroughly dried at 120 °C in a vacuum oven for 6 h. The CR2025 type coin cells were assembled in an Ar-filled glove box with O_2 content lower than 0.1 ppm using the as-prepared Si electrodes and the lithium foil as the working electrodes and the counter electrode, respectively. The electrolyte was 1M $LiPF_6$ in an iso-volume mixture of ethylene carbonate (EC) and diethyl carbonate (DEC), in which 10 wt% fluoroethylene carbonate (FEC) was added. Galvanostatic charge-discharge cycling was carried out on LAND CT-2001A in the potential range 0.01-1.2 V vs. Li/Li$^+$. The specific capacity was calculated based on the mass of Si. The charge/discharge rates were calculated with respect to the theoretical capacity of Si (1 C=4.2 Ag^{-1}). Cyclic voltammetry (CV) was performed in the potential range of 0.01-1.2 V vs. Li/Li$^+$ at a scan rate of 0.2 mV s^{-1}. Electrochemical impedance spectroscopy (EIS) measurement was performed over the frequency ranging from 0.01 to 10^5 Hz with potential amplitude of 5 mV. CV and EIS were both performed on the electrochemical workstation (PARSTAT MC).

Calculation Details: Abinito total energy and molecular-dynamics program VASP (Vienna ab initio simulation program) developed at the institutfür Material physik of the Universität Wien were used to do the calculations.[31] Pseudopotentials were described by the Generalized-gradient approximation (GGA) with the functional of Perdew, Burke and Ernzerh of (PBE). Projector augmented wave (PAW) method was used to describe the electron wave functions.[31] The kinetic energy cutoff of 400 eV and the selected k-points (5×5×5) based on the Monkhorst–Pack scheme were set. 64 atoms super-cells (Si_{64} and $Si_{63}B$) are constructed to investigate the effect of B dopant. For the substitutional-like B atoms, we replaced one of the Si atoms by B. Subsequently, we carried out a relaxation of both the atomic positions and cell shape and volume. Good convergence was obtained with these parameters and the residual forces for the relaxed atoms were less than 0.01 eV/Å.

RESULT AND DISCUSSION

Conventional doping strategy relies on vapor deposition method, which is complex and expensive. The method in this work is based on a kind of bottom-up method. Silica and boric oxides are reduced into B doped Si nano-grains. Stöber method was modified in the present study by adding boric acid. B-HPSi was obtained via a magnesiothermic reduction between Mg powder and B doped SiO_2. A schematic illustration of the synthetic paths for typical Si samples is depicted in Figure S1. The calculations on Gibbs free energy indicate that SiO_2 and boron oxide can be reduced to Si and B at 700 °C (equation 1, 2).

$$2Mg(g)+SiO_2(s,\ cristobalite)\xrightarrow{700℃}2MgO(s)+Si(s)\ \Delta G=-2.54\ KJ/mol \qquad 1$$

$$3Mg(g)+B_2O_3(l)\xrightarrow{700℃}3MgO(s)+2B(s)\ \Delta G=-77.5\ KJ/mol \qquad 2$$

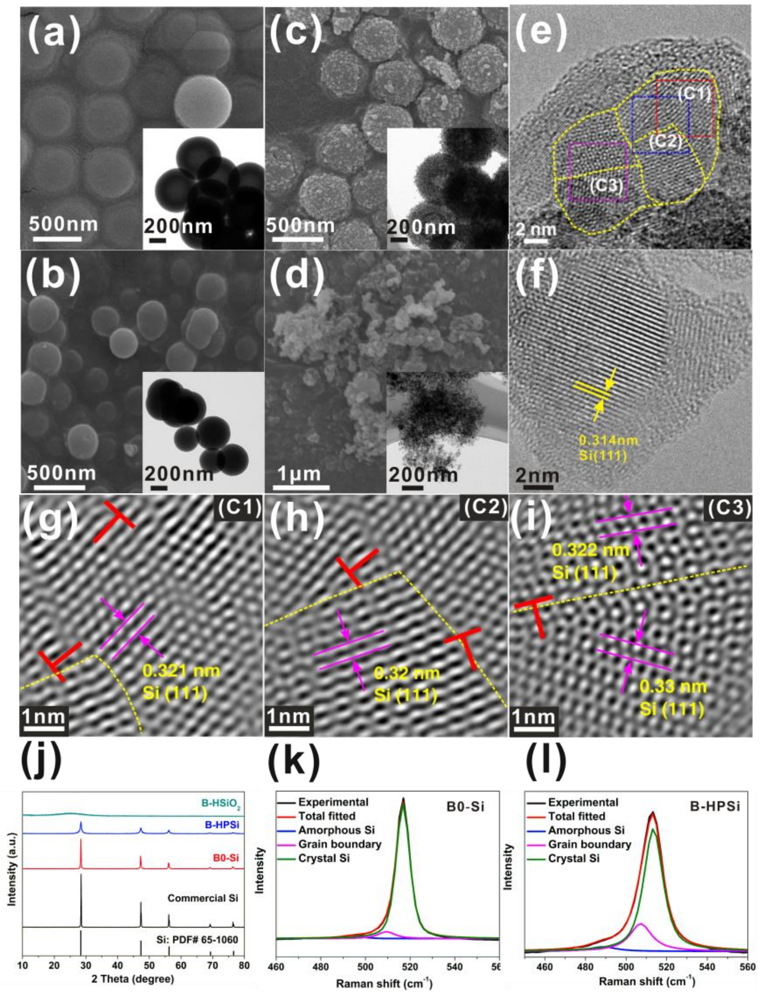

Figure 1. (a) SEM and (a inset) TEM of B-HSiO$_2$; (b) SEM and (b inset) TEM of B0-SiO$_2$; (c) SEM and (c inset) TEM of B-HPSi; (d) SEM and (d inset) TEM of B0-Si; HRTEM of (e) B-HPSi and (f) B0-Si; (g, h and i) the Fourier-filtered HRTEM images enlarged from the rectangular regions in (e) marked C1, C2, and C3; (j) XRD patterns of B-HSiO$_2$, B-HPSi, B0-Si and commercial Si; fitted Raman spectrum data of (k) B0-Si and (l) B-HPSi.

Based on ICP results, B content in B-HPSi is 0.057% (Table S1). Previous works have unambiguously demonstrated that a little content of B (at 0.001% level) could significantly change the conductivity of Si.[19] Figure 1(a) shows that the uniform smooth spherical B-HSiO$_2$ particles have the size of ~500 nm and the loose porous cores (also see Figure S2). Silica spheres without moderate B are solid spheres with diameter of 300~400 nm (Figure 1(b)). The hollow structure could be original from the inhomogeneity of SiO$_2$ during Stöber process.[32] Under the conventional Stöber synthetic conditions, TEOS undergoes inhomogeneous hydrolysis, producing partially hydrolyzed monomers with 1~4 silicon hydroxyl groups. The condensations of these monomers result in the low crosslinking degree of cores. It is speculated that B atoms also contribute to the decrease of the crosslinking degree because of their lower coordination number (Figure S3). During the etching stage, dangling bonds in core areas can facilitate the formation of hollow structures.[33] Inner cores of SiO_2 without sufficient B can be hardly etched, which could be attributed to their relatively completed O-Si framework (Figure S3).

Figure 1(c) exhibits the B-HPSi spheres having the outer diameter of ~500 nm and inner diameter of ~250 nm, which are similar to that of B-$HSiO_2$. The porous structure of B-HPSi is attributed to the removal of oxygen atoms. The enlarged TEM image of B-HPSi in Figure 1(c) inset clearly shows that B-HPSi spheres are composed of primary grains with diameter of ~10 nm (also see Figure S4). However, B-free Si (B0-Si) particles are irregular (Figure 1(d), Figure S5), which are not similar to the silica spheres. Therefore, it can be deduced that the addition of B can contribute to the maintenance of the morphology during the Mg reduction. B atoms can interfere with the Si crystallization and probably generate the robust B-Si interaction, which are much more stable than Si-Si interaction,[34] thereby enabling the structural stable B-HPSi against the harsh Mg reduction conditions. The B-HPSi materials with structural stability encourage us to explore their stability against repeated lithiation/delithiation processes.

Figure 1(e) gives the high-resolution transmission electron microscope (HRTEM) image of B-HPSi, showing local areas with deformed lattices, Several sub-grains with grain size of several nanometers are formed inside of one primary grain with grain size of ~10 nm, as indicated by the yellow lines in Figure 1(e). The deformed lattices and refined sub-grain can be hardly discovered in B0-Si sample (Figure 1(f)). Specifically, Figure 1 (g)~(i) show the Fourier-filtered atomic-scale images enlarged from the rectangular regions of B-HPSi (Figure 1(e)) marked C1, C2, and C3, respectively. The local deformed areas located on grain boundaries and the associated misfit dislocations are well indexed in the Figure 1(g)~(i). The interplanar spacings of the Si (111) planes are determined by averaged measuring the intensity profiles (see Figure S6). The results show that interplanar spacings of the Si (111) plane for the C1, C2 and C3 regions are 0.321 nm, 0.32 nm, 0.322 nm, and 0.33 nm, respectively, which are 2%~5% larger than the standard value of 0.314 nm, as indicated in Figure 1(f). Two factors could result in the local lattice expansion. Firstly, stress and strain fields result in local lattice expansion between subgrains, which is caused by thermal diffusion of dopant B atoms during the Si crystallization.[35] Secondly, size effect from nano-size grains also results in the lattice expansion. The characteristics clue in grain refining of B-HPSi can be found from the XRD patterns (Figure 1(j)). Si (111) plane peak in B-HPSi is apparently more broadened than the others (Figure S7), indicating the smaller subgrain size,[36, 37] which could be the result of stress and strain fields. The crystallinities of B0-Si and B-HPSi were quantitatively compared in Figure 1(k) and Figure 1(l) by using Raman spectrum. The fitted peaks show that B-HPSi exhibits the proportions of amorphous scattering and grain boundary scattering of ~4% and ~21%, respectively, which are quite higher than B0-Si (2% and 7%), also indicating that B-HPSi possesses many boundary atoms.[38] Based on XPS results, it is noticed that the Si_{2p} peaks shift to direction of higher binding energy (from Si standard value of 103.4 eV and 99.15 eV to B-HPSi experimental value of 103.8 eV and 99.4 eV), which can be attributed to the decrease of the electron density around Si atoms caused by the attraction of electrophilic B (Figure S8(a)). The dopant B can be confirmed by its XPS peaks shown in Figure S8(b). The nitrogen adsorption-desorption test was applied to measure the specific surface area and pore size distribution of B-HPSi (Figure S9). The BET surface area and total pore volume of B-HPSi are 130 m^2 g^{-1} and 0.68 cm^3 g^{-1}, respectively. The pore size distribution of B-HPSi ranging from 1 nm to 50 nm indicates its meso-porous and micro-porous structure, consisting with the results of TEM images in Figure1.

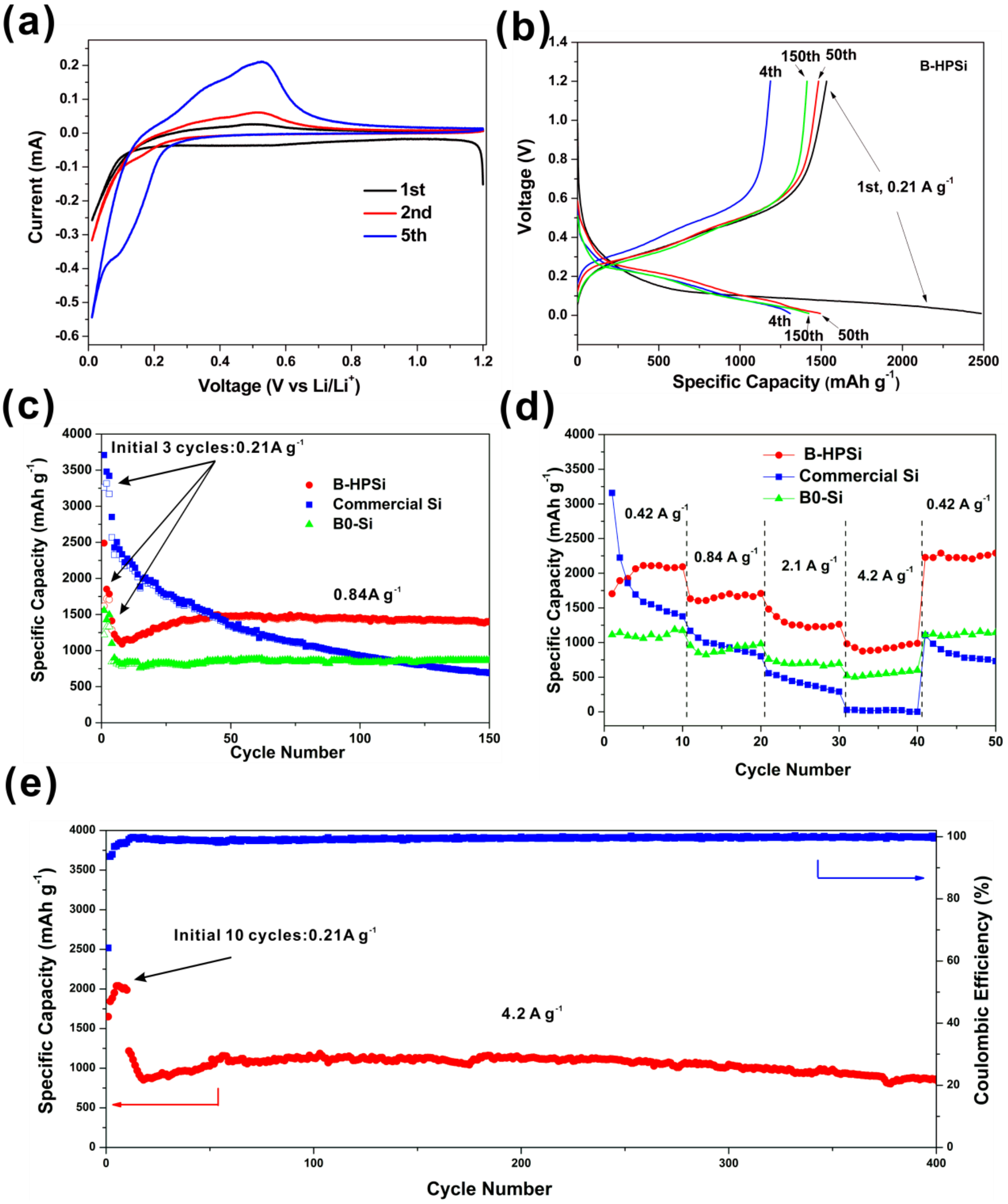

Figure 2. (a) CV curves of B-HPSi anode at a scan rate of 0.2 mV s^{-1}; (b) The charge/discharge curves of B-HPSi at 0.84 A g^{-1} (1st curves at 0.21 A g^{-1}); (c) Cyclic performance at 0.84 A g^{-1} (initial 3 cycles at 0.21 A g^{-1}) and (d) rate performance of B-HPSi, B0-Si and commercial Si; (e) Long term cycling performance of B-HPSi at 4.2 A g^{-1} (the initial 10 cycles at 0.42 A g^{-1})

Commercial Si and B0-Si were employed as reference samples for evaluating the effect of dopant B on the electrochemical performance of B-HPSi. Cyclic voltammetry (CV) test between 0.01 V and 1.2 V of B-HPSi is presented in Figure 2(a). During the initial cathodic scan, the broadened peak at 0.4~0.8 V is attributed to the formation of SEI film. The cathodic peaks at ~0.1 V and anodic peaks at 0.3~0.5

V are corresponding to the lithiation and delithiation, respectively. During the initial 5 cycles, the increase of peak current is related to the gradually electrolytic wetting of electrode. The galvanostatic discharge/charge curves of B-HPSi between 0.01 V and 1.2 V are presented in Figure 2(b), indicating the anode goes through an activation process before its final stabilization. B-HPSi, B0-Si and commercial Si are cycled at 0.84 A g^{-1} for 150 cycles after activated at 0.21 A g^{-1} for initial 3 cycles (Figure 2(c)). Though the charge capacity of commercial Si is as high as ~2600 mAh g^{-1} (4th cycle at 0.84 A g^{-1}), it suffers a rapid degradation to 1350 mAh g^{-1} in 50 cycles due to the drastic pulverization. The B0-Si electrode shows a much lower specific capacity of ~1000 mAh g^{-1}, which could be related to the poor electronic and ionic conductivity. The initial charge and discharge capacity of B-HPSi are 1600 mAh g^{-1} and 2500 mAh g^{-1}, exhibiting an initial coulombic efficiency of 64%. Relative low initial efficiency could be attributed to the abundant oxygen-containing groups in B-HPSi,[39] which can be solved by the facile pre-lithiation techniques.[40] The coulombic efficiency of B-HPSi increases to 99% in the initial 4 cycles and remains above 99% in the subsequent cycles. The charge capacity remains at ~1400 mAh g^{-1} till 150th cycle, exhibiting a retention capacity of ~93%. The influence of areal mass loading on cyclic performance of B-HPSi materials is shown in Figure S10, indicating that the as prepared materials retain ~1200 mAh g^{-1} under a mass loading as high as 1.2 mg cm^{-2}. Si materials with lower doping concentration (B1-Si and B2-Si) exhibit the gradual decrease of specific capacity with the decrease of B content (Figure S11). Moreover, B-HPSi electrode displays the best rate performance (Figure 2(d)). The reversible capacities of B-HPSi anode at 0.42 A g^{-1}, 0.84 A g^{-1}, 2.1 A g^{-1}, 4.2 A g^{-1} and 8.4 A g^{-1} are around 1800 mAh g^{-1}, 1500 mAh g^{-1}, 1250 mAh g^{-1}, 1000 mAh g^{-1} and 500 mAh g^{-1}, respectively. Since the current density returns to 0.42 A g^{-1}, a capacity of ~2000 mAh g^{-1} is recovered and remains stable in the subsequent cycles, demonstrating the robust structural stability of B-HPSi. Long term cycling test is performed at 4.2 A g^{-1} after activated at 0.42 A g^{-1} for 10 cycles (Figure 2(e)). It can be found that the B-HPSi anode exhibits an outstanding reversible capacity of ~850 mAh g^{-1} over 400 cycles. At a curent density of 8.4 A g^{-1}, B-HPSi anode also exhibits reversible capacity as high as 731.9 mAh g-1 after 300 cycles (Figure S12). Though converted into amorphous structures, the B-HPSi remains its hollow structures and subgrain boundaries after cycling (Figure S13). This indicates their excellent stability against repeated lithiation/delithiation. Therefore, the effects of the lattices deformations on ionic transporting and cyclic stability may be reserved. It should be noted that temporary capacity decrease always follows the initial activated cycles (Figure3c and e). It could be relative to internal rearrangement of anode during initial cycles. The rearrangement of active materials lead to a temporary inactivation of the active material before its normal capacity is recovered.

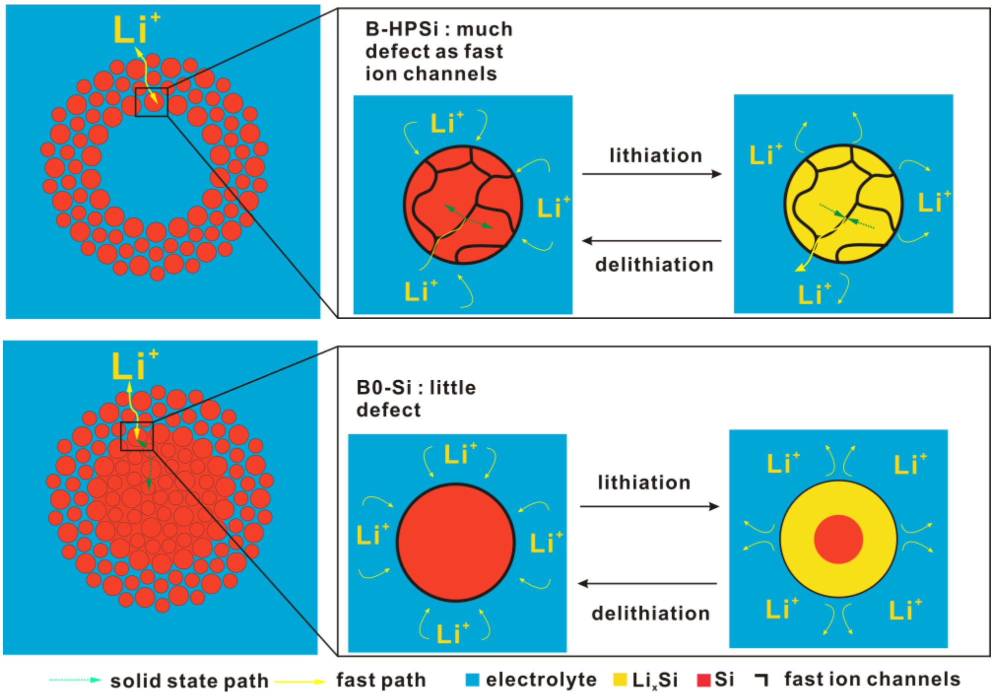

Figure 3. Hollow porous structures, local lattice deformation and refined sub-grains which act as fast ion channels.

The good performances of B-HPSi are related to the B-induced local lattice expansion, the confined subgrains and hollow porous structures, as illustrated in Figure 3. Great deal of hierarchical porous and hollow shell structures could shorten the pathway for the migration of Li ion.[14] On the other hand, pores provide reserved void for alleviating the drastic volume change during the lithiation/delithiation. The locally expanded lattice boundaries could also acts as ionic fast channels, also improving the ionic transport in the paticles.[41] B doped Si exhibit better electron conductivity than intrinsic Si (Table S1), reducing the polarization of batteries. EIS of cycled B-HPSi and B0-Si electrodes were compared to support these viewpoints, where the B-HPSi has much better electronic and ionic conductivity than the B-free one (Figure S14).

Regarding the structural stability, these pores structures provide reserved void for alleviating the drastic volume change during the lithiation/delithiation, hence stabilizing the anodic structure against repeated cycling. Besides, the interaction between B and Si could lead to the generation of B-Si atomic clusters, which could act as the frameworks that are more stable than Si-Si clusters.[34] These clusters could contribute to the stability. Based on first principle calculations, the band gaps of pure Si and B doped Si are determined as 0.89 eV and 0.58 eV, respectively (Figure S15). Agreeing with the EIS results (Figure S14) and rate capacity (Figure 2(d)), the calculated theoretical resistance decreases with the increase of B content (Table S1), suggesting the improvement of the conductivity by B doping. During the repeated lithiation/delithiation, B dopant can still improve the conductivity of Si, although the crystalline Si is completely converted to amorphous structure.[42]

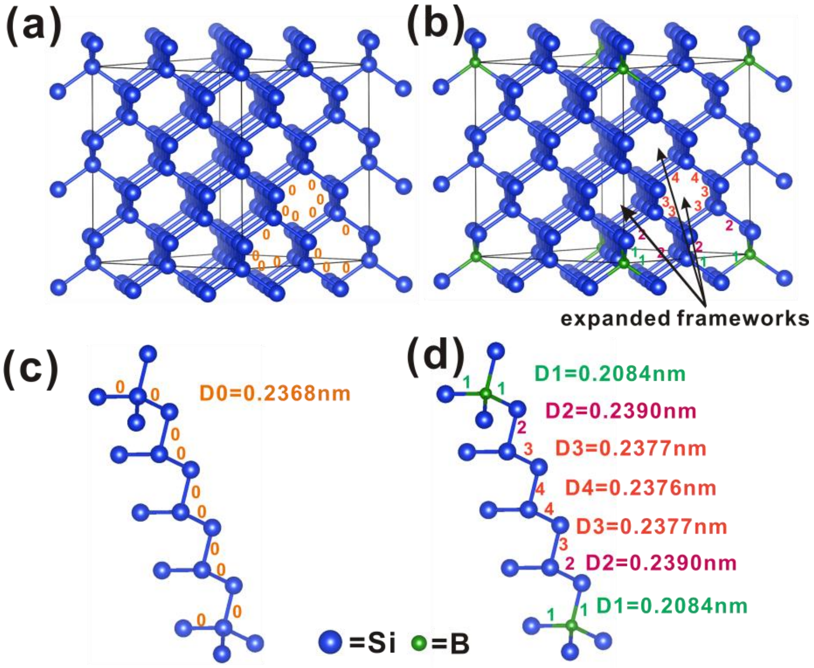

Figure 4. Simulated atomic structures of (a) pure Si and (b) B doped Si. Views of nearest-neighbor distances (D0 to D4) of (c) pure Si and (d) B doped Si. Where '0' corresponds to Si-Si distance in pure Si; '1' bond corresponds to Si-B distance; '2', '3', '4' bonds correspond to Si-Si distance gradually away from the Si-B bond, respectively.

The plots of the electronic densities on (110) planes for the pure Si and B doped Si are visualized in Figure S16. It is clearly shown that B atoms can receive electrons from Si atoms, which leads to the decrease of electronic density around Si atoms, explaining the blue shift of Si_{2p} peaks. The electron transfers from Si atoms to B atoms also result in the lattice deformation of Si, as the simulated crystallographic illustrations of pure Si and B doped Si in Figure 4 (a) and (b). Figure 4 (c) and (d) gives the detailed nearest-neighbor distances of the pure Si (D0) and the B doped Si, respectively. The nearest neighbor distance of pure Si (D0) is a constant value of ~0.2368 nm. However, B dopant atoms vary the nearest-neighbor distance. Typically, the D1 between Si and B is 0.2084 nm (14% smaller than pure Si-Si), while D2 (between the adjacent Si atoms and the sub-adjacent Si atoms) is 0.2390 nm (1% larger than pure Si-Si). D3 and D4 values of Si-Si in the areas away from B atoms gradually decrease to ~0.2376 nm which is still slightly larger than that of pure Si. The variation in nearest-neighbor distance between atoms could partially expand the frameworks of Si for improving the ionic conductivity.

CONCLUSION

In conclusion, a facile strategy in the present work for the fabrication of the B-HPSi anode with refined sub-grains and local lattice expansion is developed via a combination of co-condensation and Mg reduction. This method brings a series of positive effects. Simultaneously, the diffusion paths of B in Si could be shortened. The hollow porous structures, B dopant induces local lattice expansion and sub-grains refining are discovered, which play critical roles for improving the rate performance and cyclic stability. Other interesting findings are reported, such as the formation of hollow silica and morphological stabilization against harsh thermo-reduction. The discoveries in this work could attract wide interests in areas such as electrode materials and catalysts.

AUTHOR INFORMATION

Corresponding Authors

[a*] E-mail: j-yang@csu.edu.cn, (J. Yang)

[b*] E-mail: xsyang@polyu.edu.hk, (X. Yang)

Notes

The authors declare no competing financial interest.

ACKNOWLEDGMENT

Financial support provided by the Nature Science Foundation of China (Grant no. 51204209 and 51274240), the Project of Innovation-driven Plan in Central South University and the PolyU Departmental General Research Fund (no. G-UADK) are gratefully acknowledged. Dr. Y. Ren and Prof. X. Zhou contributed equally to this work.

Supporting Information Available: (SEM and TEM images and cyclic performance of B2-Si; detailed XRD pattern, EIS, simulated band structure, electron-density map and TEM of Si after cycles; B content and calculated electronic conductivity.). This material is available free of charge via the Internet.

REFERENCES

1. Zhao, L.; Wu, H.-H.; Yang, C.; Zhang, Q.; Zhong, G.; Zheng, Z.; Chen, H.; Wang, J.; He, K.; Wang, B.; Zhu, T.; Zeng, X. C.; Liu, M.; Wang, M.-S. Mechanistic origin of the high performance of yolk@shell Bi_2S_3@N-doped carbon nanowire electrodes. *ACS Nano* **2018,** *12*, 12597-12611.

2. Yang, Z.; Wu, H.-H.; Zheng, Z.; Cheng, Y.; Li, P.; Zhang, Q.; Wang, M.-S. Tin nanoparticles encapsulated carbon nanoboxes as high-performance anode for lithium-ion batteries. *Front. Chem.* **2018,** *6*, 533-533

3. Xiao, W.; Zhou, J.; Yu, L.; Wang, D.; Lou, X. W. Electrolytic formation of crystalline silicon/germanium alloy nanotubes and hollow particles with enhanced lithium-storage properties. *Angew. Chem.* **2016,** *55*, 7427.

4. Yoon, T.; Bok, T.; Kim, C.; Na, Y.; Park, S.; Kim, K. S. Mesoporous silicon hollow nanocubes derived from metal-organic framework template for advanced lithium-Ion battery anode. *ACS Nano* **2017,** *11*, 4808-4815.

5. Du, F. H.; Li, B.; Fu, W.; Xiong, Y. J.; Wang, K. X.; Chen, J. S. Surface binding of polypyrrole on porous silicon hollow nanospheres for Li-ion battery anodes with high structure stability. *Adv. Mater.* **2014,** *26*, 6145-50.

6. Son, Y.; Son, Y.; Choi, M.; Ko, M.; Chae, S.; Park, N.; Cho, J. Hollow silicon nanostructures via the Kirkendall effect. *Nano Lett.* **2015,** *15*, 6914.

7. Li, B.; Li, S.; Jin, Y.; Zai, J.; Chen, M.; Nazakat, A.; Zhan, P.; Huang, Y.; Qian, X. Porous Si@C ball-in-ball hollow spheres for lithium-ion capacitors with improved energy and power densities. *J. Mater. Chem. A* **2018,** *6*, 21098-21103.

8. Li, B.; Qi, R.; Zai, J.; Du, F.; Xue, C.; Jin, Y.; Jin, C.; Ma, Z.; Qian, X. Silica wastes to high-performance lithium storage materials: A rational designed Al_2O_3 coating assisted magnesiothermic process. *Small* **2016,** *12,* 5281-5287.

9. Zheng, Z.; Wu, H.-H.; Chen, H.; Cheng, Y.; Zhang, Q.; Xie, Q.; Wang, L.; Zhang, K.; Wang, M.-S.; Peng, D.-L.; Zeng, X. C. Fabrication and understanding of Cu_3Si-Si@carbon@graphene nanocomposites as high-performance anodes for lithium-ion batteries. *Nanoscale* **2018,** *10*, 22203-22214.

10. Hu, R.; Sun, W.; Chen, Y.; Zeng, M.; Zhu, M. Silicon/graphene based nanocomposite anode: Large-scale production and stable high capacity for lithium ion batteries. *J. Mater. Chem. A* **2014,** *2*, 9118-9125.

11. Sun, W.; Hu, R.; Liu, H.; Zeng, M.; Yang, L.; Wang, H.; Zhu, M. Embedding

nano-silicon in graphene nanosheets by plasma assisted milling for high capacity anode materials in lithium ion batteries. *J. Power Sources* **2014,** *268*, 610-618.

12. Sun, W.; Hu, R.; Liu, H.; Zhang, H.; Liu, J.; Yang, L.; Wang, H.; Zhu, M. Silicon/wolfram carbide@graphene composite: Enhancing conductivity and structure stability in amorphous-silicon for high lithium storage performance. *Electrochim. Acta* **2016,** *191*, 462-472.

13. Li, X.; Gu, M.; Hu, S.; Kennard, R.; Yan, P.; Chen, X.; Wang, C.; Sailor, M. J.; Zhang, J. G.; Liu, J. Mesoporous silicon sponge as an anti-pulverization structure for high-performance lithium-ion battery anodes. *Nat. Commun.* **2014,** *5*, 4105.

14. Wang, D. W.; Li, F.; Liu, M.; Lu, G. Q.; Cheng, H. M. Mesopore-aspect-ratio dependence of ion transport in rodtype ordered mesoporous carbon. *J. Phys. Chem. C* **2008,** *112*, 9950-9955.

15. Ming, H.; Qiu, J.; Zhang, S.; Li, M.; Zhu, X.; Wang, L.; Ming, J. Constructing dense SiO_X@carbon nanotubes versus spinel cathode for advanced high-energy lithium-ion batteries. *ChemElectroChem* **2017,** *20*, 337-339.

16. Wan, W.; Zhang, Q.; Cui, Y.; Wang, E. First principles study of lithium insertion in bulk silicon. *J. Phys. Condens. Mat.* **2010,** *22*, 415501.

17. Tritsaris, G. A.; Zhao, K.; Okeke, O. U.; Kaxiras, E. Diffusion of lithium in bulk amorphous silicon: A theoretical study. *J. Phys. Chem. C* **2012,** *116*, 22212–22216.

18. Tan, T. Y.; Gösele, U. Point defects, diffusion processes, and swirl defect formation in silicon. *Appl. Phys. A* **1985,** *37*, 1-17.

19. Thurber, W.; Mattis, R.; Liu, Y.; Filliben, J. Resistivity-dopant density relationship for boron-doped silicon. *J. Electrochem. Soc.* **1980,** *127*, 2291-2294.

20. Morin, F. J.; Maita, J. P. Electrical properties of silicon containing arsenic and boron. *Phys. Rev.* **1954,** *96*, 28-35.

21. Ge, M.; Rong, J.; Fang, X.; Zhou, C. Porous doped silicon nanowires for lithium ion battery anode with long cycle life. *Nano Lett.* **2012,** *12*, 2318-2323.

22. Ge, M.; Rong, J.; Fang, X.; Zhang, A.; Lu, Y.; Zhou, C. Scalable preparation of porous silicon nanoparticles and their application for lithium-ion battery anodes. *Nano Res.* **2013,** *6*, 174-181.

23. Chen, M.; Li, B.; Liu, X.; Zhou, L.; Yao, L.; Zai, J.; Qian, X.; Yu, X. Boron-doped porous Si anode materials with high initial coulombic efficiency and long cycling

stability. *J. Mater. Chem. A* **2018,** *6*, 3022-3027.

24. Han, Y.; Lin, N.; Xu, T.; Li, T.; Tian, J.; Zhu, Y.; Qian, Y. An amorphous Si material with a sponge-like structure as an anode for Li-ion and Na-ion batteries. *Nanoscale* **2018,** *10*, 3153-3158.

25. Zhou, Y.; Guo, H.; Yan, G.; Wang, Z.; Li, X.; Yang, Z.; Zheng, A.; Wang, J. Fluidized bed reaction towards crystalline embedded amorphous Si anode with much enhanced cycling stability. *Chem. Commun.* **2018,** *54*, 3755-3758.

26. Favors, Z.; Bay, H. H.; Mutlu, Z.; Ahmed, K.; Ionescu, R.; Ye, R.; Ozkan, M.; Ozkan, C. S. Towards scalable binderless electrodes: Carbon coated silicon nanofiber paper via Mg reduction of electrospun SiO_2 nanofibers. *Sci. Rep.* **2015,** *5*, 8246.

27. Zuo, X.; Xia, Y.; Ji, Q.; Gao, X.; Yin, S.; Wang, M.; Wang, X.; Qiu, B.; Wei, A.; Sun, Z.; Liu, Z.; Zhu, J.; Cheng, Y. J. Self-templating construction of 3D hierarchical macro-/mesoporous silicon from 0D silica nanoparticles. *ACS Nano* **2017,** *11*, 889-899.

28. Ren, Y.; Zhou, X.; Zhou, H.; Yang, J.; Chen, S.; Wu, L.; Nie, Y.; Wang, B. Zn-assisted magnesiothermic reduction for the preparation of ultra-fine silicon nanocrystals for lithium ion batteries. *Chem. Eng. J.* **2017,** *328*, 691-694.

29. Zhou, X.; Wu, L.; Yang, J.; Tang, J.; Xi, L.; Wang, B. Synthesis of nano-sized silicon from natural halloysite clay and its high performance as anode for lithium-ion batteries. *J. Power Sources* **2016,** *324*, 33-40.

30. Lee, S.; Park, S. S. Structure, defect chemistry, and lithium transport pathway of lithium transition metal pyrophosphates (Li2MP2O7, M: Mn, Fe, and Co): Atomistic simulation study. *Chem. Mater.* **2012,** *24*, 3550–3557.

31. Kresse, G.; Joubert, D. From ultrasoft pseudopotentials to the projector augmented-wave method. *Phys. Rev. B Condens. Mat.* **1999,** *59*, 1758-1775.

32. Yi, J. W.; Zhu, L.; Wei, S. T.; Yan, W. T.; Yang, Y.; Wang, C.; Chen, H. Revisiting the stober method: Inhomogeneity in silica shells. *J. Am. Chem. Soc.* **2011,** *133*, 11422-11425.

33. Liang, Z.; Zhuang, Z.; Zhao, H.; Lin, M.; Zhao, D.; Mai, L. Intricate hollow structures: Controlled synthesis and applications in energy storage and conversion. *Adv. Mater.* **2017,** *29*, 1602914.

34. Ushio, J.; Nakagawa, K.; Miyao, M.; Maruizumi, T. Surface segregation behavior of B, Ga, and Sb during Si MBE: Calculations using a first-principles method. *Phys. Rev. B* **1998,** *58*, 3932-3936.

35. Cowern, N. E. B.; Theunissen, M. J. J.; Roozeboom, F.; Berkum, J. G. M. V. Boride-enhanced diffusion in silicon: Bulk and surface layers. *Appl. Phys. Lett.* **1999,** *75*, 181-183.

36. Bernard, M. C.; Cortes, R.; Keddam, M.; Takenouti, H.; Bernard, P.; Senyarich, S. Structural defects and electrochemical reactivity of β-Ni(OH) 2. *J. Power Sources* **1996,** *63*, 247-254.

37. Delmas, C.; Tessier, C. Stacking faults in the structure of nickel hydroxide: A rationaleof its high electrochemical activity. *J. Mater. Chem.* **1997,** *7*, 1439-1443.

38. Yue, G.; Lorentzen, J. D.; Lin, J.; Han, D.; Wang, Q. Photoluminescence and Raman studies in thin-film materials: Transition from amorphous to microcrystalline silicon. *Appl. Phys. Lett.* **1999,** *75*, 492-494.

39. Zhou, X.; Ren, Y.; Yang, J.; Ding, J.; Zhang, J.; Hu, T.; Tang, J. Si nanoflake-assembled blocks towards high initial coulombic efficiency anodes for lithium-ion batteries. *Chem. Commun.* **2018,** *54*, 12214-12217.

40. Liu, N.; Hu, L.; Mcdowell, M. T.; Jackson, A.; Cui, Y. Prelithiated silicon nanowires as an anode for lithium ion batteries. *Acs Nano* **2011,** *5*, 6487-6493.

41. Bordes, A.; Vito, E. D.; Haon, C.; Boulineau, A.; Montani, A.; Marcus, P. Multiscale investigation of silicon anode Li insertion mechanisms by time-of-flight secondary ion mass spectrometer imaging performed on an in situ focused ion beam cross section. *Chem. Mater.* **2016,** *28*. 1566-1573.

42. Robertson, J. Dopant states in a-Si: H. II. Effects of H and F. *Phys.Rev. B* **1983,** *28*, 4658-4665.

Supporting Information

Boron-Doped Spherical Hollow-Porous Silicon Local Lattice Expansion toward a High-Performance Lithium-Ion-Battery Anode

Yongpeng Ren,[†] *Xiangyang Zhou,*[†] *Jingjing Tang,*[†] *Jing Ding,*[†] *Song Chen,*[†] *Jiaming Zhang,*[†] *Tingjie Hu,*[†] *Xu-Sheng Yang,*[*,‡] *Xinming Wang,*[§] *and Juan Yang,*[*,†]

[†] School of Metallurgy and Environment, Central South University, Changsha 410083, China.
[‡] Advanced Manufacturing Technology Research Centre, Department of Industrial and Systems Engineering, The Hong Kong Polytechnic University, Hung Hom, Kowloon, Hong Kong, China
[§] School of Materials Science and Engineering, Xiangtan University, Xiangtan, China

*Corresponding author.

* E-mail: xsyang@polyu.edu.hk, (X. Yang)
* E-mail: j-yang@csu.edu.cn, (J. Yang)

$$\rho_{Si} = \frac{1.305\times10^{16}}{N} + \frac{1.133\times10^{17}}{N\times\left[1+\left(N\times2.58\times10^{-9}\right)^{-0.737}\right]} \qquad \text{S1}$$

ρ_{Si}, resistivity of B doped crystal Si, Ω cm
N, atomic density of boron atom in Si, cm^{-3}

Table S1 B contents in Si and SiO_2 based on ICP-AES measurements and the calculated resistivity values

	B contents In SiO_2(wt%)	B contents In Si (wt%)	Atomic density of B (cm^{-3})	Resistivity (Ω cm)
B0	<0.001	<0.001	$\sim5\times10^{17}$	~0.22
B1	0.038	0.014	0.18×10^{20}	5.48×10^{-3}
B2	0.093	0.029	0.38×10^{20}	2.86×10^{-3}
B-HPSi ($B-HSiO_2$)	0.16	0.057	0.74×10^{20}	1.55×10^{-3}
Saturated solution of B (theoretical value)	—	0.17%	2.2×10^{20}	5.49×10^{-4}

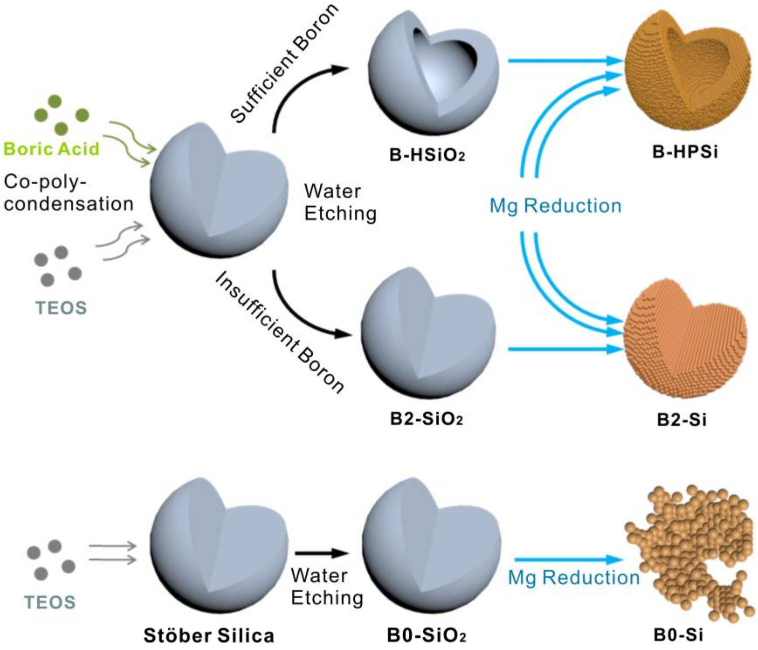

Figure S1. Synthetic paths of B-HPSi, B2-Si and B0-Si

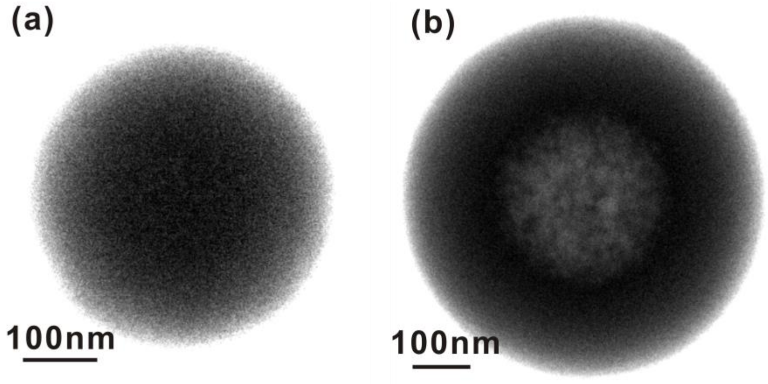

Figure S2. Contrast adjusted TEM images of (a) solid silica spheres without boron addition (B0-SiO_2) and (b) hollow spheres with proper boron addition (B-$HSiO_2$)

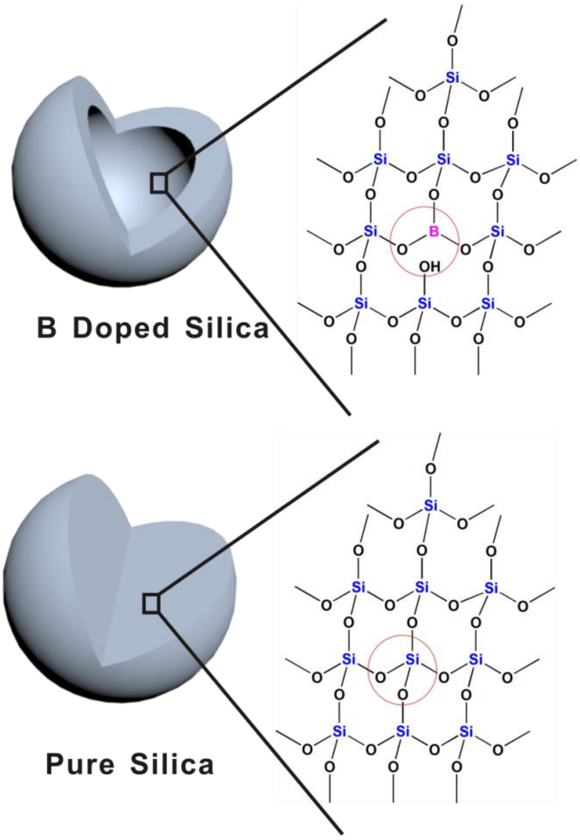

Figure S3. Illustration of a boron atom with lower coordination number in Si-O framework

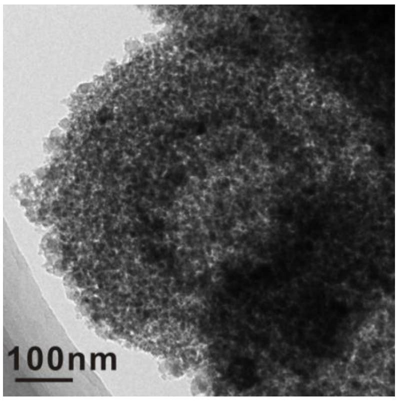

Figure S4. Enlarged TEM image of B-HPSi

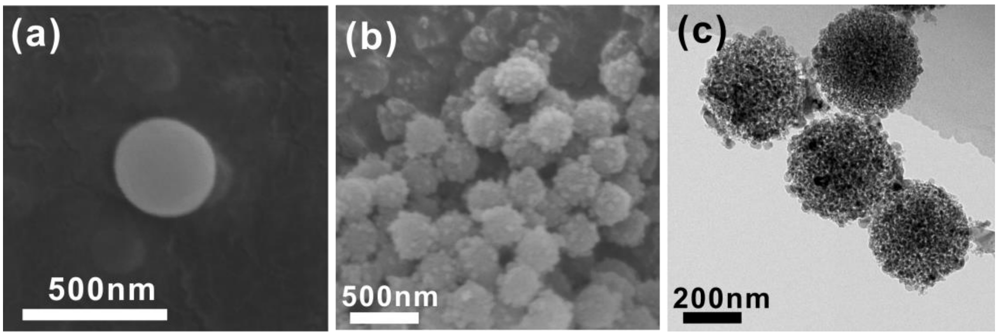

Figure S5. SEM images of (a) B2-SiO_2, (b) B2-Si and (c) TEM image of B2-Si

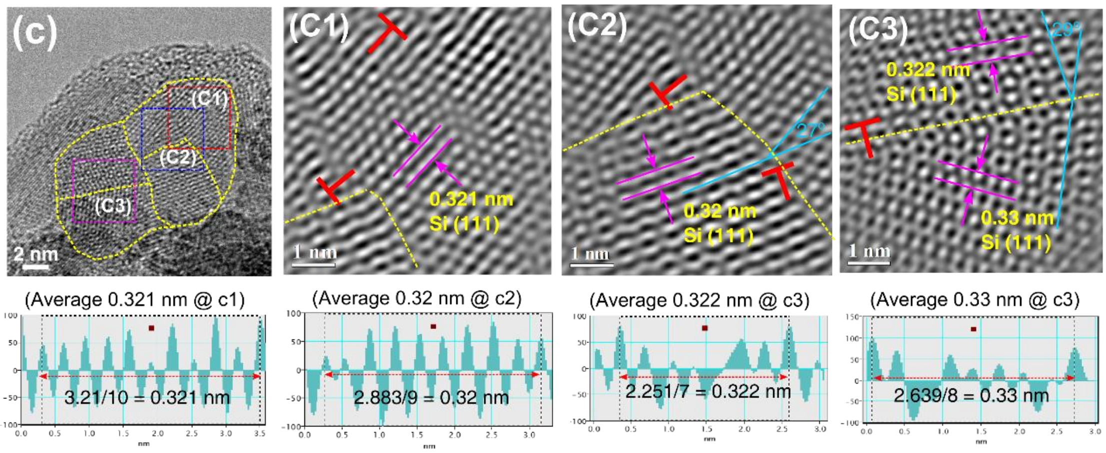

Figure S6. HRTEM image of B-HPSi (c) and the Fourier-filtered HRTEM images (C1-C3) enlarged from the rectangular regions marked C1, C2, and C3 in (c); and the corresponding the intensity profiles for measuring the interplanar spacing of Si (111) planes.

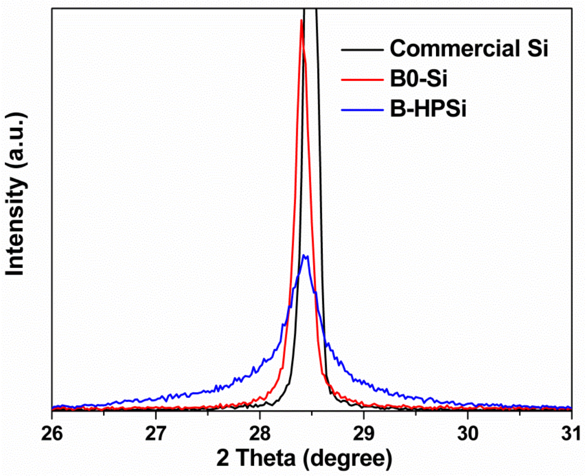

Figure S7. Detailed XRD patterns of B-HPSi, B0-Si and commercial Si

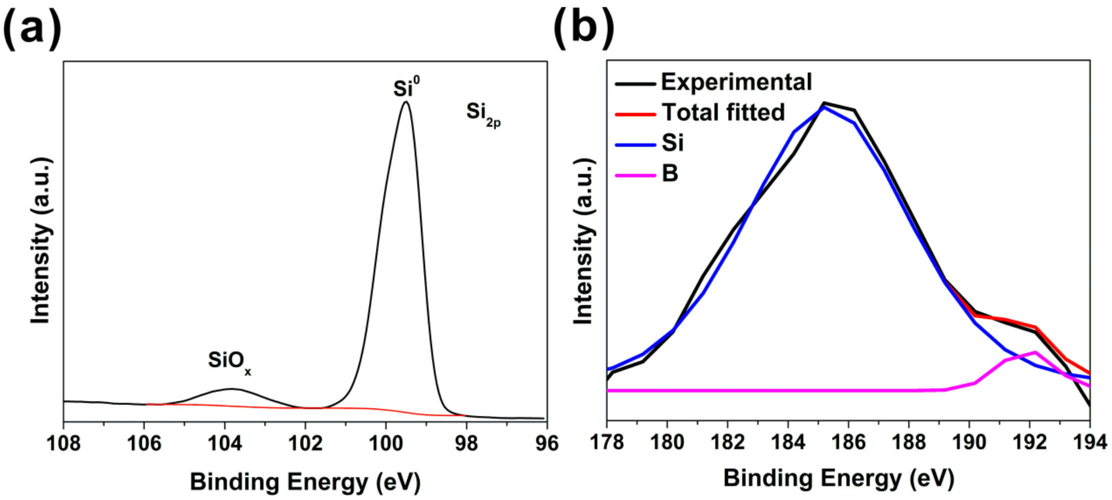

Figure S8. (a) Si and (b) B peaks of XPS of B-HPSi

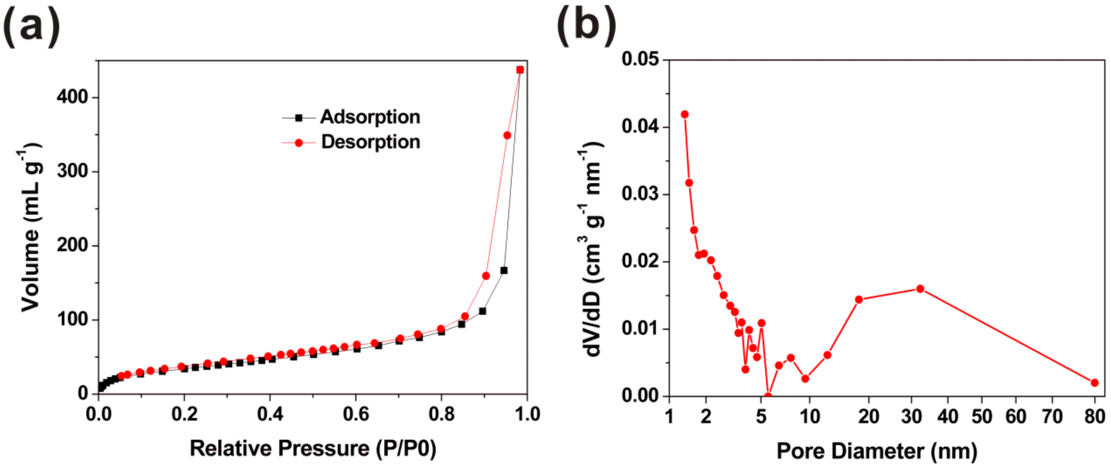

Figure S9. N2 adsorption/desorption data (a) and differential pore size distribution (b) of B-HPSi

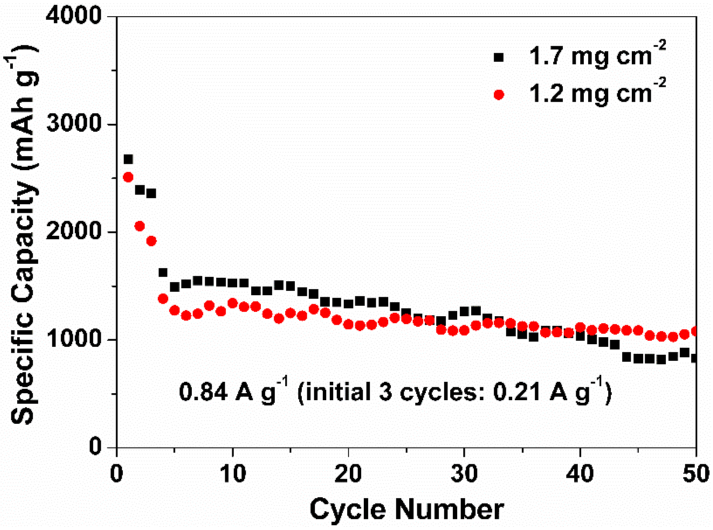

Figure S10. Cyclic performances of B-HPSi under areal mass loading of 1.2 mg cm^{-2} and 1.7 mg cm^{-2}

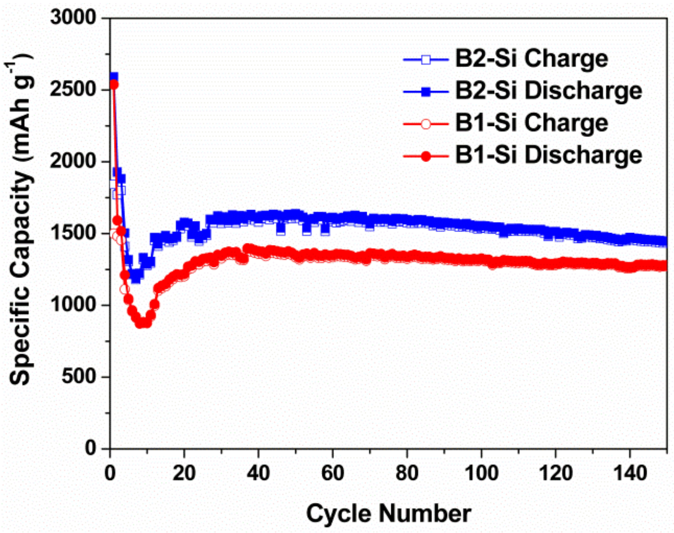

Figure S11. Cycle performances at 0.84A g^{-1} of B1-Si and B2-Si (activated at 0.21 A g^{-1} for the initial 3 cycles)

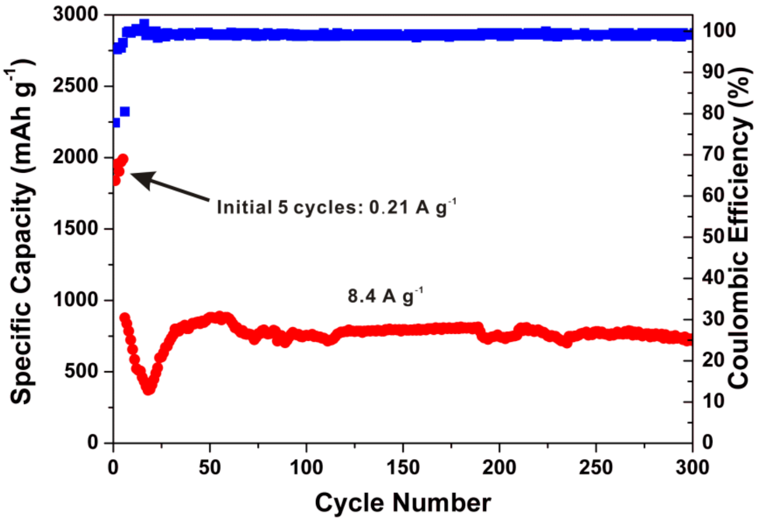

Figure S12. Cyclic performances of B-HPSi at 8.4 A g^{-1} (activated at 0.21 A g^{-1} for the initial 5 cycles)

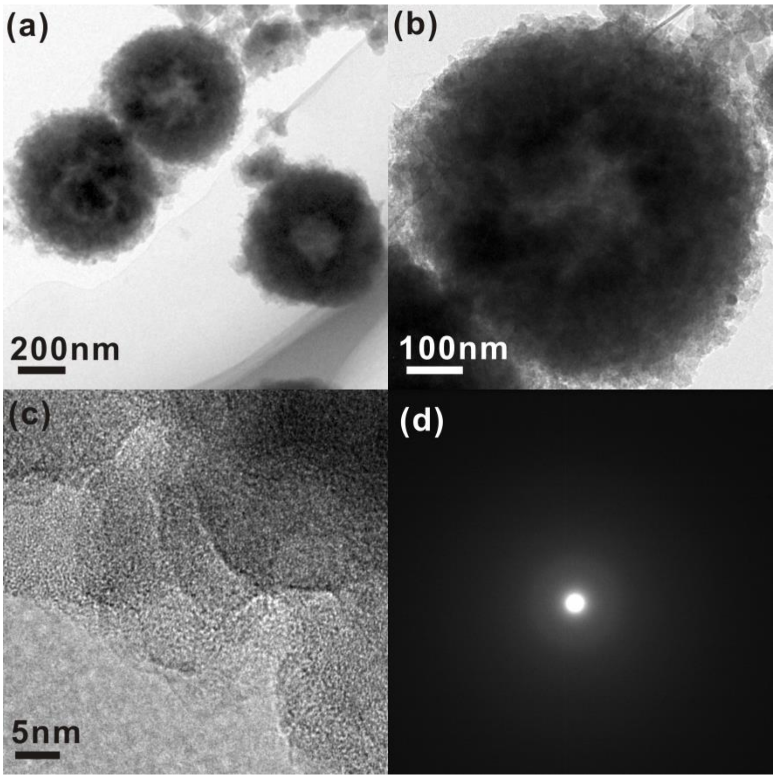

Figure S13. TEM (a) and (b), HRTEM (c) and SAED (d) of B-HPSi anode obtained after cycling

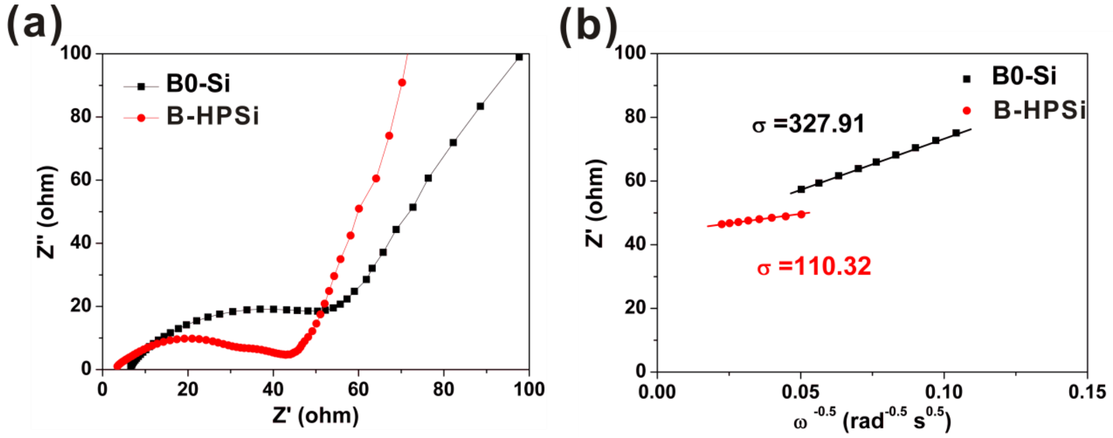

Figure S14. Nyquist plots (a) and Warberg coefficients (b) of B-HPSi and B0-Si

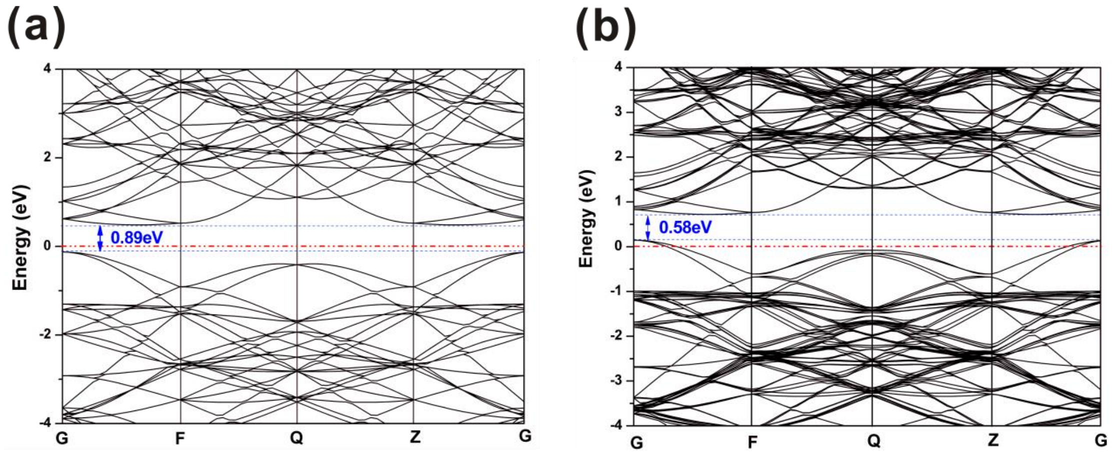

Figure S15. Simulated band structure of pure Si (a) and B-doped Si (b)

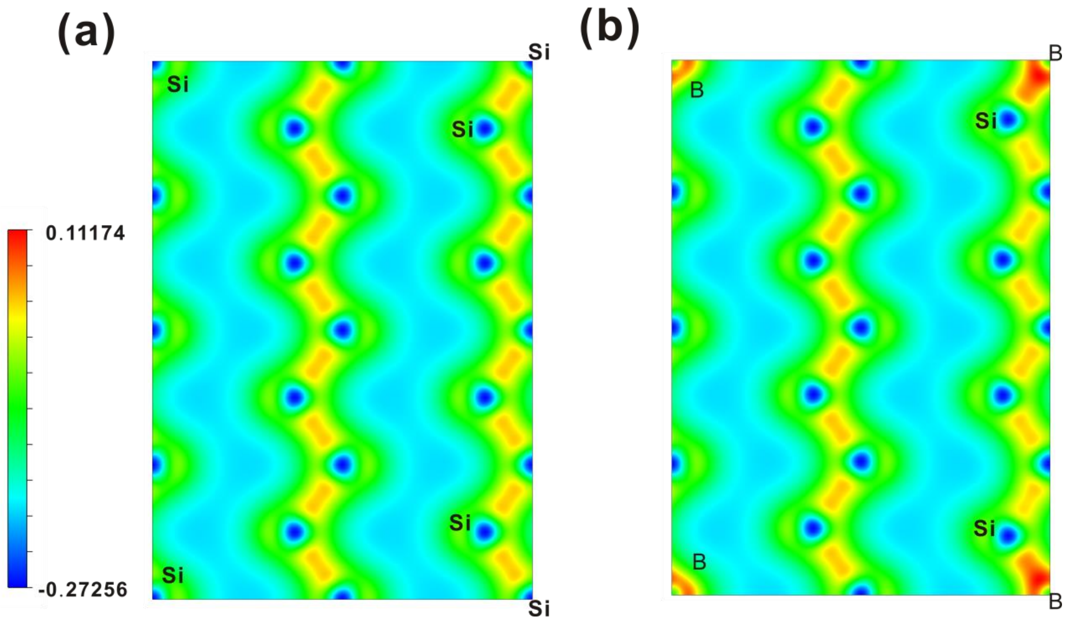

Figure S16. Simulated charge density plots of pure Si (110) (a) and B doped Si (110) (b)